Contribution of magnetic measurement methods to the analysis of iron sulfides in archaeological waterlogged wood-iron assemblies

Céline Remazeilles, Francois Leveque, Egle Conforto, Laure Meunier, Philippe Refait

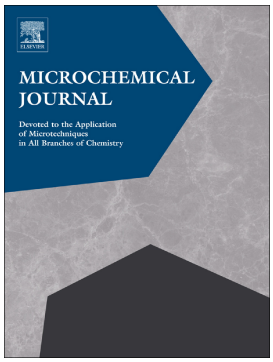

Contribution of magnetic measurement methods to the analysis of iron sulfides in archaeological waterlogged wood'iron assemblies

Céline Rémazeilles, François Lévêque, Egle Conforto, Laure Meunier, Philippe Refait

PII: S0026-265X(19)30603-4
DOI: https://doi.org/10.1016/j.microc.2019.04.062
Reference: MICROC 3876

To appear in: *Microchemical Journal*

Received date: 12 March 2019
Revised date: 23 April 2019
Accepted date: 23 April 2019

Please cite this article as: C. Rémazeilles, F. Lévêque, E. Conforto, et al., Contribution of magnetic measurement methods to the analysis of iron sulfides in archaeological waterlogged wood'iron assemblies, Microchemical Journal, https://doi.org/10.1016/j.microc.2019.04.062

Contribution of magnetic measurement methods to the analysis of iron sulfides in archaeological waterlogged wood-iron assemblies

Céline Rémazeilles[a]*, François Lévêque[b], Egle Conforto[a], Laure Meunier[c], Philippe Refait[a]

[a] LaSIE, Laboratory of Engineering Sciences for the Environment, UMR 7356 CNRS-La Rochelle University, Avenue Michel Crépeau, F-17042 La Rochelle cedex 1, France

[b] LIENSs, Littoral, Environment and Societies, UMR 7266 CNRS- La Rochelle University, 2 rue Olympe de Gouges, F-17000 La Rochelle, France.

[c] Arc-Nucléart, 17 Avenue des Martyrs F-38054 Grenoble cedex 9, France

* Corresponding author : Céline Rémazeilles : Tel: +33 5 46 45 83 52; Fax: +33 5 46 45 82 41; E-mail: cremazei@univ-lr.fr

Abstract

Pyrite and greigite were identified in the wood of two ancient shipwrecks using an original multi-technique analytical approach. Structural characterization methods such as environmental scanning electron microscopy, micro-Raman spectroscopy and X-ray diffraction were combined with magnetic measurement methods, such as magnetic susceptibility measurements and isothermal remanent magnetization acquisition curves. This is the first time that magnetic measurement methods are used in the field of cultural heritage to study wet organic archaeological materials. They proved to be particularly suitable to detect with a very high sensitivity ferromagnetic *s.l.* mineral phases inside waterlogged wooden samples, i.e. in the bulk. The occurrence of iron sulfides in archaeological shipwrecks extracted from waterlogged environments is usually attributed to microbiologically influenced

corrosion of iron fasteners. This study demonstrates that the nature of the identified iron sulfides is consistent with a step-by-step *in situ* anoxic oxidation process of mackinawite.

Keywords: Pyrite, greigite, Raman spectroscopy, ESEM, magnetic characterization, archaeological shipwrecks.

1. Introduction

The durability of wood-iron assemblies can be problematic if a structure, or part of it, is waterlogged. This issue is well known in the field of cultural heritage preservation. When pieces of wood are assembled with iron fasteners (nails) and remain in wet and anoxic conditions, microbiologically influenced corrosion (MIC) of the metal is likely to take place, a consequence of the metabolic activity of sulfide-producing bacteria (SPB) [1-4]. These anaerobic microorganisms can use the oxygenated species of sulfur (sulfates, thiosulfates, sulfites…) present in the environment as electron acceptors and convert them to sulfides. The latter tend to precipitate with Fe^{2+} ions resulting from the *in situ* corrosion of the iron fasteners, which leads to the formation of iron sulfides [5]. These compounds constitute a diverse group of solids with various crystalline forms, Fe/S ratios and oxidation levels for both iron and sulfur. When corrosion of iron takes places in presence of sulfides, mackinawite ($Fe^{II}S$) is the iron sulfide that precipitates from the dissolved species. It is however metastable and can be transformed to more stable mineral compounds [6-9]. It may also be oxidized, in both aerated and anoxic conditions. Fig. 1 summarizes the oxidation processes of mackinawite, based on bibliographic data. The transformation pathways depend on oxic/anoxic feature of the environment, sulfur supply via the production of sulfide species, temperature, moisture, pH, etc. [6-21]. As far as waterlogged wood-iron assemblies are concerned, these processes, occurring *in situ* or after exposure to air, strongly influence the

degradation mechanisms of wood. For instance, the post-excavation exposition to air and the drying of the wood-iron assemblies leads to the precipitation of voluminous iron/sulfate-containing crystals such as melanterite ($FeSO_4,7H_2O$), rozenite ($FeSO_4,4H_2O$) or natrojarosite ($NaFe_3(OH)_6(SO_4)_2$). These compounds appear as unsightly efflorescence on the surface of the wood and are responsible of mechanical stresses, cracks and embrittlement [22-26]. Moreover, iron sulfides oxidation is concomitant to a high acidification, which is a crucial issue for holocellulose preservation. Macromolecules of wood, especially cellulose and hemicelluloses, are actually highly sensitive to acid hydrolysis and oxidation, which can induce the decay of the organic matrix [27-29]. Historical shipwrecks such as the *Vasa* (17^{th} century), the *Batavia* (17^{th} century) or the *Mary Rose* (16^{th} century) are affected by these degradation phenomena. Various iron sulfides and reduced sulfur species were identified in archaeological remains. Pyrite (FeS_2) and α-S_8 sulfur are generally considered as the most common compounds. Organic sulfur was detected in thiols (R-SH) and disulfides (R-SS-R') groups associated to molecules of wood [22-26,30-32]. Mackinawite (FeS) proved predominant in wood samples extracted from 18^{th} and 19^{th} centuries shipwrecks, with greigite (Fe_3S_4) present in smaller amount [33]. Marcasite (FeS_2) and pyrrhotite ($Fe_{1-x}S$) were also mentioned [23,33]. These few examples show that the iron sulfides present inside the wood may differ from one wreck to another.

This article is focused on the analysis of mineral phases, especially iron sulfides, in wood-iron artefacts. The samples were extracted from two ancient shipwrecks excavated from waterlogged soils, namely the wreck of Mandirac (Narbonne, France) and LSG4 (for Lyon Saint-Georges n°4, Lyon, France). No conservation treatment was applied to the analyzed samples. The new results are compared to those obtained previously with other shipwrecks (*USS Monitor* and wrecks of La Natière) [33]. Our approach aims to examine samples using a combination of various analytical techniques. The originality of the present work is to

associate magnetic measurement methods such as magnetic susceptibility measurement and isothermal remanent magnetization (IRM) acquisition curves with more common elemental and structural analysis methods, such as micro-Raman spectroscopy, scanning electron microscopy coupled with energy dispersive spectroscopy and X-ray diffraction. Some iron sulfides are magnetically ordered and can be easily detected and identified via magnetic characterization methods, even if present in very small amount (< 1 ppm). Magnetic measurements methods are very sensitive, allow analysis in the bulk and are not hindered nor perturbed by organic matter and water. Because they are based on the magnetic properties of mineral phases, they are in a first approach limited to the detection of magnetic phases. Common "non-magnetic" methods can detect a wider range of minerals, inform about their crystal structure and morphology but are much less sensitive. This is the first time that magnetic measurement methods are used in the field of cultural heritage to characterize organic archaeological materials.

The ferromagnetic greigite was systematically detected in the analyzed samples thanks to magnetic measurements methods. Pyrite, which is paramagnetic, was detected in large amounts by other methods. The occurrence of both phases is discussed in relation to the oxidation pathways of mackinawite (FeS) and parameters like oxygen concentration and pH, duration of the burial and microbiological activity. The relevance of the applied analytical procedure is also assessed.

2. Materials and methods

2.1. Origin of the samples

Two shipwrecks excavated from waterlogged sediments were studied.

The wreck of Mandirac (4th century) was discovered in the site of Castelou/Mandirac corresponding to the ancient ports of Narbonne (France), now inland [34-36]. The dimensions

were estimated at about 12 m long and 4 m wide. A Magnetic prospecting campaign conducted on site in 2014 revealed that the wood was abnormally magnetic throughout the entire wreck. It was also determined that there was no more metal in the nails used for assembly. Therefore, the magnetic signal had to be attributed to magnetic corrosion products present inside the wood. A plank was extracted during excavation and dedicated to the present study. This plank is called *vaigre 11*, in accordance with the inventory of each element of the wreck carried out by the archaeologists. *Vaigre 11* was about 80 cm long, 16.5 cm wide, 2.5 cm thick and contained a nail. No restoration treatment was applied to this plank.

LSG4 (2^{nd} century), for Lyon Saint-Georges wreck n°4, is one of the 16 wrecks excavated between 2002 and 2004 in the city of Lyon (France) along the Saône river [37]. It was about 19 m long for 5 m wide. During the ten years that elapsed between the excavation and the restoration treatment (PEG impregnation, Arc-Nucleart laboratory), the wreck was kept immersed in a lake. Four wood fragments of various shape, about 5 centimeters long, were provided for the study. Their localization in the wreck was unknown. Like the plank *vaigre 11*, they were not treated for restoration purpose.

2.2. Analytical procedure

To avoid the oxidation of Fe(II) compounds sensitive to oxidation by O_2 from air, it is necessary to keep the samples waterlogged between excavation/extraction and analysis. Our samples were then carried to the laboratory wrapped in a plastic film or in bags placed in airtight containers filled with water. After reception at the laboratory, they were kept in their original packaging and stored in a freezer (-24°C) until analysis. Freezing can damage the wood, but this procedure proved efficient to avoid the transformation of oxygen-sensitive mineral phases such as iron sulfides [38, 39]. During the analysis campaign, they were stored at 4°C in order to prevent growth of mold.

The analytical procedure was designed for the study of large samples, such as *vaigre 11*, i.e. a wooden plank of several decimeters long. The first step consisted in determining the gradient of the magnetic properties in the whole sample by performing magnetic susceptibility measurements (contact measurements). Each measurement represented an elementary volume of 25 cm^2 (elementary surface) x 2 cm (thick). Thus, the sample was gridded in rows and columns. Values were measured and a magnetic susceptibility mapping was performed. The elementary surface was named according to its row/column position. The sample was then cut into 1.9x1.9x1.9 cm^3 cubes (with a circular saw equipped with a Teflon blade or with a ceramic knife). Each cube was supposed to be extracted from each elementary volume. The cubes were placed in a plastic box adapted to the sample holder of the apparatus and magnetic susceptibility was measured before IRM and backfield curves were acquired. Magnetic characterization methods allow analyzing the whole volume of the cubes and were used first for this reason.

Once magnetic measurements were performed, surface analysis methods were used to characterize some cubes selected for interest. For each cube, the surface of a freshly cut slice, randomly chosen according to the radial, tangential or longitudinal direction, was examined first with a stereomicroscope. The cutting was carried out with a ceramic blade in order to the contamination of the samples by magnetic micro-particles possibly provided by a steel blade. Such contamination could perturb further magnetic measurements. Then, Environmental Scanning Electron Microscopy coupled with Energy Dispersive Spectroscopy (ESEM/EDS), micro-Raman spectroscopy (μ-SR) and X-ray diffraction (XRD) experiments were performed on other slices and conducted without any special protection against air. In addition, pH measurements were carried out on another slice still wet. The cutting of slices was carried out prior to observation/analysis and was renewed for each method and only the side

corresponding to the inner part of the sample was analyzed, so that always a freshly cut surface unexposed to air was studied.

Vaigre 11 extracted from the wreck of Mandirac was studied using the procedure described above. For the small samples extracted from LSG4, it was not relevant to determine a gradient of magnetic properties and the analysis started with the IRM acquisition curves.

Table 1 lists several naturally occurring iron sulfides with relevant properties. Each of these compounds could be expected a priori. Magnetic characterization methods and micro-Raman spectroscopy are part of the analytical procedure described above, so magnetic data and Raman bands are reported in this table [14,15,40-49]. Iron oxides such as magnetite (Fe_3O_4) and maghemite (γ-Fe_2O_3) are included because of their magnetic properties and their possible presence as corrosion products in the studied samples.

2.3. Methods

Low field magnetic susceptibility was measured with a magnetic susceptibility meter SM30 (ZH Instruments, www.zhinstruments.com) for contact measurement and with a KLY4 (Agico, www.agico.com) magnetic susceptibility meter for bulk samples. IRM and backfield curves were acquired up to three Tesla with a MMPM10 Magnetic Measurements pulse magnetizer (Magnetic Measurements Ltd., www.magnetic-measurements.com) and measured with a JR6 (Agico) spinner magnetometer. The magnetic susceptibility presents a wide range of variation over three orders of magnitude from negative values to strong positive ones. An arbitrary constant of 25×10^{-6} is added in order to proceed to a $\log_{10}$ transform. This allows considering only the para- and ferro-magnetic *sensu lato (s.l.)* components, removing the diamagnetic ones (*i.e.* wood and water).

Electronic high-resolution micrographs and elemental analysis spectra were obtained with a scanning electron microscope (Quanta 200 FEG/ESEM, FEI, www.fei.com) coupled with an

EDAX Genesis EDS system for X-Ray microanalysis (www.edax.com). The observations were performed in environmental mode, low pressure (0.002 atm), with an acceleration voltage varying between 15 and 20 kV. This experimental method does not require any preparation for non-conductive materials and samples of wood were placed still wet in the analysis chamber.

Micro-Raman spectroscopy experiments were carried out with a High Resolution LabRAM HR spectrometer (Jobin Yvon, www.horiba.com) equipped with a microscope (Olympus BX41, www.olympus-global.com), a ×50 objective and a Peltier-based cooled charge coupled device detector. The laser power was lowered down to 0.6 mW in order to prevent the transformation of heat-sensitive mineral phases. Spectra were recorded with the LabSpec software at a resolution of 0.2 cm^{-1}. The samples were analyzed with an excitation wavelength of 632.82 nm.

In complement, X-ray diffraction experiments were performed directly on the wood. A freshly cut slice was placed in the sample holder and exposed to the X-ray beam (wavelength $\lambda_{Co\text{-}K\alpha}$ = 0.17903 nm). The diffractometer used (INEL EQUINOX 6000, www.inel.fr) is equipped with a curved detector (CPS 590) designed for the simultaneous detection of the diffracted photons on a 2θ range of 90°. Acquisition was made with a constant angle of incidence (5 degrees) during 30 minutes. The diffraction patterns were processed with the Match! software (Cristal Impact, www.crystalimpact.com) including the COD database (Crystallography Open Database).

Finally, pH measurements were performed on wet wooden slices freshly cut from the samples with a surface electrode (Sentix Sur, WTW, www.wtw.com) calibrated using pH = 4.00 and pH = 7.00 buffer solutions (VWR, www.vwr.com).

3. Results

For the sake of clarity, magnetic measurements techniques are called "magnetic methods" while μ-SR, ESEM/EDS and XRD are called together "classical methods".

3.1. Identification of iron sulfides in vaigre 11 (wreck of Mandirac)

The entire plank *vaigre 11,* extracted from the wreck of Mandirac and containing the remains of an iron nail, showed magnetic enhancement compared to natural wood and water values. Fig. 2a is the superimposition of the picture of the plank with the corresponding magnetic susceptibility mapping. According to the color code, red and white/light pink correspond to intense magnetic enhancement; blue or purple correspond to low values. The most magnetic zone is centered on the nail, which is located at position g20. Thirteen white squares are represented and correspond to the cubic samples that were analyzed by combining magnetic and classical methods. They were chosen along line e and column 20 because the most magnetic spot was located in e20 position. Only cubes e4, e15 and h20 are described in this article as representative examples. The remanent hysteresis curves of these three samples are very similar (Fig. 2b) and are characteristic of greigite. The greigite content, which was extrapolated from theoretical remanent saturation magnetization (Ms = 59 Am^2/kg; Mrs/Ms = 0.12) [50], ranges from 0.3 to 6000 ppm. Grain size can be determined with remanent curves and was estimated at about 20-500 nm. ESEM micrographs in chemical contrast obtained from the same three sample cubes are presented in Fig. 2c. In each case, bright crystals are observed. The micrograph of cube e4 reveals small crystals scattered in what appear like tracheids. In cube e15, particles of submicron to ten microns size are agglomerated inside the fibers. In the most magnetic area, where cube h20 was extracted, well-formed framboïds are observed. Framboïdal pyrite corresponds to equigranular submicron to micron-sized crystals of pyrite densely packed in spherical clusters. They were also found in large amount in cubes e20, f20, g20 (not shown). It must be noted that framboïdal pyrite was present in higher

density around the nail. EDS analysis of these bright micro-sized or framboïdal crystals (not shown) confirmed that they were composed of sulfur and iron with an average Fe/S atomic ratio equal to 0.51 ± 0.04 (the calibration was carried out using a reference sample of natural pyrite external to the present corpus). This ratio corresponds to a FeS_2 stoichiometry, matching with pyrite or marcasite. Raman spectra (Fig. 3a,b,c) and XRD patterns (Fig. 3d,e,f) of cubes e4, e15 and h20 demonstrate that both pyrite (Raman bands at 344, 380 and 430 cm^{-1}) and marcasite (Raman bands at 323 and 386 cm^{-1}) [46,47] are present. Marcasite was mainly detected in cubes e4 and e5 (e5 not shown), while pyrite was predominant elsewhere. In the most magnetic zone, greigite was also identified by μ-RS (Raman bands at 138, 188, 250, 350 and 365 cm^{-1}) [15]. At last siderite ($FeCO_3$) was identified in samples g20 and h20 (Raman bands at 185, 283, 715 and 1085 cm^{-1}). The iron nail located in the cube g20 was completely corroded into siderite and pyrite. Therefore, cube h20 right next to it could contain part of its corrosion products.

3.2 Identification of iron sulfides in LSG4 samples

Four samples extracted from LSG4 wreck were analyzed. Backfield IRM curves are shown in Fig. 4a. Mid-magnetization, revealed by the intersection with the abscissa axis, is observed at 60-63 mT for two samples and 28-35 mT for two others. The first value corresponds to greigite and the second results from a mixture of maghemite or magnetite and greigite. Figs. 4b,c,d correspond to an ESEM micrograph, a Raman spectrum and the diffraction pattern obtained from the same sample. Numerous micron-sized and octahedral bright crystals are observed in chemical contrast (Fig. 4b). EDS spectra (not shown) revealed that these crystals were composed of sulfur and iron with an average Fe/S atomic ratio equal to 0.50 ± 0.02. This value, associated to the shape of the microcrystals, the Raman spectrum (Fig. 4c) and the diffraction pattern (Fig. 4d), are typical of pyrite.

3.3 Morphologies of pyrite

The pyrite grains present inside the wood of LSG4 and the wreck of Mandirac exhibit the two typical morphologies of pyrite: framboïdal and euhedral. The term framboïd originates from the French word framboise (raspberry), because of its granular appearance reminiscent of this fruit. The size of the observed framboïds was between a few microns to more than 20 μm. Euhedral pyrite corresponds to well-formed crystals with flat faces and sharp angles. In our samples, crystals of euhedral pyrite are mainly octahedral. Fig. 5 gathers the different morphologies of FeS_2 crystals observed in samples from both wrecks. Fig. 5a shows a crystal with a radiative growth, detected in the wreck of Mandirac (cube e4). This shape is typical of marcasite [51]. Figs. 5b-h correspond to pyrite showing a range of different shapes, mainly cubes and octahedrons, truncated or not. Both wrecks presented the same diversity. In the plank of Mandirac, the morphologies changed with the distance from the nail. Framboïds were rather concentrated around the nail and could be observed in very high density around it (Fig. 2c). Euhedral crystals were observed farther from the nail (distance > ~5 cm). The density of crystals was sometimes very high in the tracheids, so that the concretions, by growing, took the shape of the cells (e.g. Fig. 5f).

3.4 Additional results

Needle-like crystals composed of sulfur, oxygen and calcium were often observed in the samples extracted from both wrecks (Fig. 6). They correspond to gypsum ($CaSO_4.2H_2O$) identified by μ-RS (Fig. 3c, cube h20, main Raman band at 1015 cm^{-1}, *vaigre 11*) and XRD (Fig. 3g, cube h20, *vaigre 11* and Fig. 5, LSG4). Besides, a strong signal attributed to the wood appears as broad humps located at 18.7° and 26.7° or 32.6° on the diffraction patterns of Fig. 3d,e,f, Fig. 4d and of Fig. 6c.

The pH values measured on the samples extracted from LSG4 were low, comprised between 2.4 and 3.7 from a fragment to another. In *vaigre 11*, the pH varied with distance from the cube e20 (i.e. the most magnetic cube of the plank). In the most magnetic area (Magnetic susceptibility > 6.0 10^{-4} SI with maximum value of 53.9 10^{-4} SI), the pH values were comprised between 2.6 and 3.5. The weakest value of 2.6 corresponded to the cube g20 containing the nail. Then, the pH increased gradually away from the nail to reach a value of 5.6 at position e3 (less magnetic area, Magnetic susceptibility < 6.0 10^{-4} SI with lowest value of -0.093 10^{-4} SI).

4. Discussion

4.1 Oxidation processes of the precursor mackinawite (FeS)

Pyrite and greigite are the predominant iron sulfides inside the wood fragments of LSG4 and in *vaigre 11* of the wreck of Mandirac. ESEM micrographs showed that these minerals were located in the pores and vessels of the wood. Mackinawite was not detected, while this phase was predominant in wood samples extracted from more recent shipwrecks dated from the 18th and 19th centuries [33]. Marcasite was detected in the wreck of Mandirac and observed rather far from the nail. Besides, gypsum ($CaSO_4$. $2H_2O$) was also observed. This phase resulted probably from the precipitation of salts, as the wood dried during analysis. Finally, neither pyrrhotite nor smythite were detected. These phases are ferromagnetic and magnetic methods are extremely sensitive. It was consequently considered that they were not present or at least as traces compared to greigite.

Pyrite and greigite were identified here as the main iron sulfides while mackinawite was predominating in samples of other wrecks [33]. The previously studied wrecks were extracted from marine sites, while LSG4 was excavated from fluvial sediments and the wreck of

Mandirac from a coastal marshland. In any case, the occurrence of iron sulfide is supposed to be associated with the MIC process of the fasteners. Huisman et al. [52] reported the presence of pyrite in several wooden samples extracted from different waterlogged sites, marine or terrestrial. Sulfate reducing bacteria, the main microorganisms involved in MIC processes of iron, can grow and be active in various environments and various reducing conditions whatever the salinity, i.e. in seawater, freshwater or sediments. Nevertheless, the diversity of iron sulfides from one wreck to another can result from the influence of many parameters. Among them time, i.e. age of the wrecks, and pH of the medium seem particularly interesting to point out.

First, the older the wreck is, the longer it has remained in anoxic conditions once trapped in sediments, provided that the environment was never disturbed overtime. The wrecks reported in Rémazeilles et al. [33] were more recent (19^{th} and 18^{th} centuries) than LSG4 and the wreck of Mandirac (2^{nd} and 4^{th} centuries). Referring to Fig. 1, mackinawite is the first product resulting from sulfide assisted corrosion of iron. In anoxic conditions and without excess of sulfides, mackinawite may not transform. In an excess of sulfide is provided, mackinawite (1 Fe atom for 1 S atom) can be oxidized into greigite (1 Fe atom for 1.3 S atoms). Then, greigite can in turn be oxidized into pyrite (1 Fe atom for 2 S atoms). This pathway would occur with a persistent sulfide supply, i.e. typically in the presence of a continuous sulfide-producing bacteria activity. A long-term microbiological activity promoted by a bacterial consortium is possible in a waterlogged archaeological site because anoxic conditions can be maintained for a very long time. The anoxic oxidation of mackinawite into pyrite via greigite involves a progressive assimilation of sulfide species in the solid phases, so that the environment does never reach the overdose level in sulfides able to impede the development of SRB colonies. In addition to this, sulfide species can also react with organic matter in disulfides or thiols molecular groups for example. Thus, the predominance of pyrite and

greigite in LSG4 and in the wreck of Mandirac may be associated with an intense and/or very long microbiological activity. Since greigite was detected in LSG4 samples and in *vaigre 11*, its implication in the oxidation process of mackinawite into pyrite is unambiguous, in particular concerning the formation of framboïdal pyrite. Wilkin and Barnes proposed a model describing the formation process of framboïdal pyrite from precipitation of mackinawite and implying greigite as the pyrite precursor [53]. This model involves four steps and can be perfectly transposed to the current system as follows: (i) precipitation of mackinawite due to MIC promoted by SPB, (ii) oxidation of mackinawite into greigite by H_2S provided by the anaerobic bacterial activity, (iii) aggregation of greigite microcrystals due to their magnetic properties, (iv) oxidation of greigite into pyrite microcrystals by bacterial H_2S. Once formed, framboïds continue to grow and produce coarser and less ordered clusters. The ancient LSG4 and Mandirac wrecks illustrate step (iv) that corresponds to the transformation of greigite into pyrite. Consequently, mackinawite has already been entirely oxidized into greigite. In more recent wrecks, mackinawite was predominant because it was not completely transformed. It can be assumed that mackinawite was also the first iron sulfide to precipitate, due to the MIC of iron fasteners, in LSG4 and in the wreck of Mandirac.

Secondly, the anoxic oxidation process of iron sulfides, occurring *in situ*, is concomitant to an acidification of the medium. LSG4 and *vaigre 11* samples, containing greigite and pyrite, presented accordingly very low pHs. On the contrary, the pHs measured on the samples reported in Rémazeilles et al. [33], containing mainly mackinawite, were closed to neutrality.

The oxic pathway of iron sulfides oxidation, as reported in Fig. 1, specifies that greigite can be oxidized into iron (oxyhydr)oxides and mineral sulfur (α-S_8) when oxygen is present. Magnetite was detected by magnetic methods in LSG4 samples. Its formation is attributed to the 10 years long storage in the lake between excavation and restoration. The occurrence of iron oxides can be explained by the exposure of the remains to an aqueous oxygenated

medium and the aerial oxidation of greigite by dissolved O_2. Moreover, once the remains were immersed in the lake, the on-going MIC process of the nails could have been converted into a process exclusively controlled by O_2, favoring the occurrence of iron oxides (e.g. magnetite) as corrosion products instead of iron sulfides. Magnetite was not detected in *vaigre 11*, which was stored sheltered from air as soon as it was excavated and all along its storage before analysis.

4.2. Focus on greigite and contribution of magnetic measurement methods

Magnetic measurements performed on LSG4 and *vaigre 11* samples demonstrated that the magnetic signal was mainly due to greigite. That of *vaigre 11* was actually exclusively due to greigite. This compound could be detected in the entire plank by magnetic measurement methods, while classical methods revealed its presence only close to the nail (cubes e17, e18, e19, e20, f20, g20, h20). Because the same magnetic signal was detected all along the wreck, it can be concluded that the whole wreck was contaminated by greigite. As a diagnosis and in term of representativeness of the analyzed part of the remains, such results are very useful for restorers to design a relevant conservation strategy.

Fig. 7 displays two SEM micrographs of areas where greigite was identified by Raman spectroscopy. Fig. 7a was obtained from a sample of LSG4 and Fig. 7b was obtained from cube e18 of *vaigre 11*. In both cases, aggregates of submicron to micron-sized platelets were observed. The morphology of greigite is not always clearly described in literature [43] but the platelet shape visible in the figure was already reported for a hydrothermally synthesized greigite [54]. The EDS spectrum presented in Fig. 7c was obtained from the particles of Fig. 7a. It is only composed of iron and sulfur peaks and the Fe/S atomic ratio proved different from that of pyrite and varied from 0.76 to 0.80. This is slightly higher than 0.75, the expected

value for greigite (Fe_3S_4), and could correspond to a non-stoichiometric greigite with general formula $Fe_{3+x}O_4$.

Greigite is particularly interesting because it occurs as an intermediate compound either during the anoxic oxidation process of mackinawite into pyrite or during the oxidation by air of mackinawite into mineral sulfur and iron (oxyhydr)oxide (see diagram of Fig. 1). Consequently, the detection of this phase is crucial for the understanding of the evolution processes of iron sulfides in natural environments and of the (long-term) effects of MIC.

Greigite may however be particularly difficult to detect with surface micro-analysis methods like SEM or micro-Raman spectroscopy when it is present in small amount and scattered in samples. In contrast, magnetic measurement techniques allow analyzing samples in the bulk with a very low detection limit (less than ppm). Using these techniques, we were able to identify greigite unambiguously, as well as to demonstrate the absence of pyrrhotite and smythite. However, magnetic methods restrain the detection of mineral species to magnetic ones. This is not the case for the other methods allowing potentially the detection of a wider range of minerals. Magnetic methods are also hardly applicable in the presence of metallic iron (α-Fe) that gives rise to a very intense signal likely to mask the less intense signals due to other species. Therefore, due the respective potentialities and limits of each method used in the methodological approach developed in this article, their combination is crucial for a reliable and exhaustive detection of iron sulfides.

5. Conclusion

The corrosion of iron fasteners used for assembly led to the occurrence of iron sulfides in the wood of two archaeological shipwrecks (2^{nd} and 4^{th} century) extracted from waterlogged soils. Greigite and pyrite, predominant in both wrecks, are assumed to result from the microbiologically influenced corrosion (MIC) of the fasteners. Considering the burial context

of the wrecks, these phases may have formed *in situ* over time by anoxic oxidation of mackinawite, a process promoted by a long-term sulfide producing microbial activity. This implies that mackinawite was certainly the first MIC corrosion product formed on the iron fasteners in the early times of the burial. Mackinawite was not detected in the samples because it has more likely been completely transformed into greigite and pyrite.

Greigite is interesting to consider because of its central role in different transformation processes of mackinawite. Because of it is a magnetically ordered compound, the use of magnetic measurement methods is particularly suitable for its detection inside waterlogged wood samples.

Acknowledgements

Corinne Sanchez (Archeology of Mediterranean Societies, UMR-5140 CNRS / University of Montpellier 3 / Ministry of Culture and Communication / Labex Archimedes), Marie-Pierre Jézégou (DRASSM) are warmly thanked for letting us bringing a plank from the wreck of Mandirac. Many thanks are also addressed Marine Crouzet (Arc-Nucléart) for providing the samples of LSG4.

We also thank Nicolas Plasson and Maylis Minjacq (students) and Guillaume Lotte (LaSIE) for their contribution to analyses.

This research did not receive any specific grant from funding agencies in the public, commercial, or not-for-profit sectors.

Declarations of interest: none

References

1 H.A. Videla, W.G. Characklis, Biofouling and Microbiologically Induced Corrosion, Int. Biodeter. Biodegr. 29 (1992) 195-212.

2 W. Lee, W.G. Charaklis, Corrosion of mild steel under anaerobic biofilm, Corrosion 49 (1993) 186-199.

3 P. Angell, Understanding Microbially Influenced Corrosion as Biofilm-mediated Changes in Surface Chemistry, Curr. Opin. Biotechnol. 10 (1999) 269-272.

4 I.B. Beech, J. Sunner, Biocorrosion: Towards Understanding Interactions Between Biofilms and Metals, Curr. Opin. Biotechnol. 15 (2004) 181-186.

5 R.G.J. Edyvean, Hydrogen Sulfide – A Corrosive Metabolite, Int. Biodeterior. 27 (1991) 109-120.

6 D. Rickard, G.W. Luther, Chemistry of iron sulfides, Chem. Rev. 107 (2007) 514-562.

7 S. Pineau, R. Sabot, L. Quillet, M. Jeannin, Ch. Caplat, I. Dupont-Morral, Ph. Refait, Formation of the Fe(II-III) hydroxysulphate green rust during marine corrosion of steel associated to molecular detection of dissimilatory sulphite-reductase, Corros. Sci. 50 (2008) 1099-1111.

8 M. Langumier, R. Sabot, R. Obame-Ndong, M. Jeannin, S. Sablé, Ph. Refait, Formation of Fe(III)-containing mackinawite from hydroxysulphate green rust by sulphate reducing bacteria, Corros. Sci. 51 (2009) 2694-2702.

9 I. Lanneluc, M. Langumier, R. Sabot, M. Jeannin, Ph. Refait, S. Sablé, On the bacterial communities associated with the corrosion product layer during the early stages of marine corrosion of carbon steel, Internat. Biodeter. Biodegr. 99 (2015) 55-65.

10 L.G. Benning, R.T. Wilkin, H.L. Barnes, Reaction pathways in the Fe-S system below 100°C, Chem. Geol. 167 (2000) 25-51.

11 S. Boursiquot, M. Mullet, M. Abdelmoula, J.-M. Génin, J.J. Ehrhardt, The dry oxidation of tetragonal FeS_{1-x} mackinawite, Phys. Chem. Miner. 28 (2001) 600–611.

12 M. Wolthers, L. Charlet, P.R. Van Der Linde, D. Rickard, C.H. Van Der Weijden, Surface chemistry of disordered mackinawite (FeS), Geochim. Cosmochim. Ac. 69 (2005) 3469-3481.

13 D. Rickard, The solubility of FeS. Geochim. Cosmochim. Ac. 70 (2006) 5779-5789.

14 J.-A. Bourdoiseau, M. Jeannin, R. Sabot, C. Rémazeilles, Ph. Refait, Characterisation of mackinawite by Raman spectroscopy: Effects of crystallisation, drying and oxidation, Corros. Sci. 50 (2008) 3247–3255.

15 J.-A. Bourdoiseau, M. Jeannin, C. Rémazeilles, R. Sabot, Ph. Refait, The transformation of mackinawite into greigite studied by Raman spectroscopy, J. Raman Spectrosc. 42 (2011) 496-504.

16 S. Hunger, L.G. Benning, Greigite: a true intermediate on the polysulfide pathway to pyrite, Geochem. T. 8 (2007) 1-20.

17 D. Rickard, G.W. Luther., Kinetics of pyrite formation by the H_2S oxidation of iron (II) monosulfide in aqueous solutions between 25 and 125°C: The mechanism, Geochim. Cosmochim. Ac. 61 (1997) 135-147.

18 R.M. Garrels, M.E. Thompson, Oxydation of pyrite by iron sulfate solutions, Am. J. Sci. 258 (1960) 57-67.

19 W. Stumm, J. J. Morgan, Aquatic chemistry: an introduction emphasizing chemical equilibria in natural waters, Wiley-Interscience, New York, 1981.

20 P.J. Sullivan, K.J. Reddy, J.L. Yelton, Iron sulfide oxidation and the chemistry of acid generation, Environ. Geol. Water S. 11 (1988) 289-295.

21 J.D. Rimstidt, D.J. Vaughan, Pyrite oxidation: A state-of-the-art assessment of the reaction mechanism. Geochim. Cosmochim. Ac. 67 (2003) 873-880.

22 M. Sandström, F. Jalilehvand, I. Persson, U. Gelius, P. Frank, I. Hall-Roth, Deterioration of the Seventeenth-century Warship Vasa by Internal Formation of Sulphuric Acid, Nature 415 (2002) 893–897.

23 I.D. Mac Leod, C. Kenna, Degradation of Archaeological Timbers by Pyrite: Oxidation of Iron and Sulphur Species, In: P. Hoffmann, (Ed.) Proceedings of the 4th ICOM Group on Wet Organic Archaeological Materials Conference, Bemerhaven, (1990) 133-141.

24 M. Sandström, F. Jalilehvand, I. Persson, U. Gelius, P. Frank, Acidity and Salt Precipitation on the Vasa; The Sulfur Problem, In: P. Hoffmann, J.-A. Spriggs, T. Grant, et al., (Eds.) Proceedings of the 8th ICOM Group on Wet Organic Archaeological Materials Conference, Stockholm (2001) 67-90.

25 M. Sandström, F. Jalilehvand, E. Damian, Y. Fors, U. Gelius, M. Jones, M. Salomé, Sulfur Accumulation in the Timbers of King Henry VIII's Warship Mary Rose: A Pathway in the Sulfur Cycle of Conservation Concern, P. Natl Acad. Sci. USA 102 (2005) 14165-14170.

26 Y. Fors, M. Sandström, Sulfur and iron in shipwrecks cause conservation concerns, Chem. Soc. Rev. 35 (2006) 399-415.

27 Emery, J.A., Schroeder H.A., 1974. Iron-Catalyzed Oxidation of Wood Carbohydrates. Wood Science and Technology 8, 123-137.

28 Edwards, K.J., Schrenk, M.O., Hamers, R., Banfield, J. F., 1998. Microbial oxidation of pyrite: Experiments using microorganisms from an extreme acidic environment. American Mineralogist 83, 1444-1453.

29 Farber, E., 1954. Chemical Deterioration of Wood in the Presence of Iron. Industrial and Engineering Chemistry 46, 1968-1972.

30 K.M. Wetherall, R.M. Moss, A.M. Jones, A.D. Smith, T. Skinner, D.M. Pickup, S.W. Goatham, A.V. Chadwick, R.J. Newport, Sulfur and Iron Speciation in Recently

Recovered Timbers of the Mary Rose revealed via X-Ray Absorption Spectroscopy, J. Archaeol. Sci. 35 (2008) 1317-1328.

31 I. Godfrey, V. Richards, I. MacLeod, The Batavia – Past, Current and future conservation. In: M. Ek, (Ed.) Proceedings of the Chemistry and preservation of waterlogged wooden shipwrecks conference, Shipwrecks 2011. Stockholm: Royal Institute of technology (2011) 22-28.

32 Y. Fors, H. Grudd, A. Rindby, F. Jalilehvand, M. Sandström, I. Cato, L. Bornmalm, Sulfur and iron accumulation in three marine-archaeological shipwrecks in the Baltic Sea: The Ghost, the Crown and the Sword, Sci. Rep. 4, 4222; DOI:10.1038/srep04222 (2014).

33 C. Rémazeilles, K. Tran, E. Guilminot, E. Conforto, P. Refait, Study of Fe(II) sulfides in waterlogged archaeological wood. Stu. Conserv. 58 (2013) 297-307.

34 M.P. Jézégou, J. Cavéro, M. Druez, H. Günter-Martin, V. Mathé, C. Sanchez, K. Storch, A geo-archaeological research about the Roman Harbours of Narbonne : earth and underwater survey and GIS, In : J. Henderson (Ed.) IKUWA 3 Beyond Boundaries, Proceedings of the 3rd International Congress on Underwater Archaeology, London 2008 (2012) 299-307.

35 C. Sanchez, C. Faïsse, M.P. Jézégou, V. Mathé, Le système portuaire de Narbonne antique : approche géoarchéologique, In : L. Mercuri, R. González, F. Bertoncello (Eds.), Implantations humaines en milieu littoral Méditerranéen : facteurs d'installation et processus d'appropriation de l'espace, de la Préhistoire au Moyen Âge, Actes des 24ème rencontres internationales d'archéologie et d'histoire d'Antibes, (2014) 125-136.

36 V. Mathé, C. Sanchez, G. Bruniaux, A. Camus, J. Cavero, C. Faisse, M.-P. Jézégou, J. Labussière, F. Lévêque, Prospections géophysiques multi-méthodes de structures portuaires antiques à Narbonne (Aude, France), ArcheoSciences-Rev A 40 (2016) 47-63.

37 G. Ayala, Lyon. Évolution d'un bord de Saône de l'Antiquité à nos jours : la fouille du

Parc Saint-Georges, Bilan préliminaire, Rev Archeol-Est 56 (2007) 153-185.

38 Ph. Refait, A.-M. Grolleau, M. Jeannin, E. François, R. Sabot, Localized corrosion of carbon steel in marine media: galvanic coupling and heterogeneity of the corrosion product layer, Corros. Sci. 111 (2016) 583-595.

39 Ph. Refait, A.-M. Grolleau, M. Jeannin, E. François, R. Sabot, Corrosion of carbon steel at the mud zone/seawater interface: mechanisms and kinetics, Corros. Sci. 130 (2018) 76-84.

40 C. Avril, V. Malavergne, R. Caracas, B. Zanda, B. Reynard, E. Charon, E. Bobocioiu, F. Brunet, S. Borensztajn, S. Pont, M. Tarrida, F. Guyot, Raman spectroscopic properties and Raman identification of CaS-MgS-MnS-FeS-Cr_2FeS_4 sulfides in meteorites and reduced sulfur-rich systems, Meteorit. Planet. Sci. 48 (2013) 1415–1426.

41 M.J. Dekkers, Magnetic properties of natural pyrrhotite Part I: Behaviour of initial susceptibility and saturation-magnetization related rock-magnetic parameters in a grain-size dependent framework, Phys. Earth Planet. In. 52 (1988) 376-393.

42 T.P. Mernagh, A.G. Trudu, A laser Raman microprobe study of some geologically important sulfides minerals, Chem. Geol. 103 (1993) 113-127.

43 A.P. Roberts, L. Chang, C.J. Rowan, C-S. Horng, F. Florindo, Magnetic properties of sedimentary greigite (Fe_3S_4): An update, Rev. Geophys. 49, RG1002, (2011) doi :10.1029/2010RG000336.

44 M.J. Dekkers, H.F. Passier, M.A.A. Schoonen, Magnetic properties of hydrothermally synthesized greigite (Fe_3S_4) II. High- and low-temperature characteristics, Geophys. J. Int. 141 (2000) 809–819.

45 V. Hoffmann, H. Stanjek, E. Murad, Mineralogical, magnetic and Mössbauer data of smythite (Fe_9S_{11}), Stud. Geophys. Geod. 37 (1993) 366-381.

46 A. Lopez, R.L. Frost, Raman spectroscopy of pyrite in marble from Chillagoe, Queensland, J. Raman Spectrosc. 46 (2015) 1033-1036.

47 H.D. Lutz, B. Müller, Lattice Vibration Spectra. LXVIII. Single-Crystal Raman Spectra of Marcasite-type Iron Chalcogenides and Pnictides, FeX_2 (X=S, Se, Te; P, As, Sb). Phys. Chem. Miner. 18 (1991) 265-268.

48 V. Mathé, F. Levêque, Trace magnetic minerals to detect redox boundaries and drainage effects in a marshland soil in western France Trace magnetic minerals to detect redox boundaries and drainage effects in a marshland soil in western France, Eur. J. Soil. Sci. 56 (2005) 737-751.

49 M. Hanesch, Raman spectroscopy of iron oxides and (oxy)hydroxides at low laser power and possible applications in environmental magnetic studies, Geophys. J. Int. 177 (2009) 941-948.

50 L. Chang, A.P. Roberts, Y. Tang, B.D. Rainford, A.R. Muxworthy, Q. Chen, Fundamental magnetic parameters from pure synthetic greigite (Fe_3S_4), J. Geophy. Res. 113 (2008) 1-16.

51 G.N. White, J.B. Dixon, R.M. Weaver, A.C. Kunkle, Genesis and morphology or iron sulfides in gray kaolins. Clay Clay Miner. 39 (1991) 70-76.

52 D.J. Huisman, M.R. Manders, E.I. Kretschmar, R.K.W.M. Klaassan, N. Lamersdorf, Burial conditions and wood degradation at archaeological sites in the Netherlands, Int. Biodeter. Biodegr. 61 (2008) 33-44.

53 R.T. Wilkin, H.L. Barnes, Formation processes of framboidal pyrite, Geochim. Cosmochim. Ac. 61 (1997) 323-339.

54 S. Horiuchi, H. Wada, T. Moori, Morphology and imperfection of hydrothermally synthesized greigite (Fe_3S_4), J. Cryst. Growth 24/25 (1974) 624-626.

Figures captions

Figure 1: Structural evolution and oxidation processes of mackinawite in anoxic conditions and in aerated conditions.

Figure 2: (a) Picture of *vaigre 11* (wreck of Mandirac) with superimposed magnetic susceptibility mapping (the squares correspond to analysed samples - the square with the cross corresponds to the location of the nail). (b) Magnetic remanence curves of samples e4, e15 and h20 (red) compared to remanence curves obtained from all analysed samples (grey). (c) ESEM micrographs of samples e4, e15 and h20 (chemical contrast).

Figure 3: Raman microspectroscopy spectra (a, b, c) and diffraction patterns (d, e, f) of samples e4, e15 and h20 (*vaigre 11*, wreck of Mandirac). Ma = marcasite, P = pyrite, Gy = gypsum, Si = siderite and G = greigite.

Figure 4: (a) Magnetic remanence curves obtained from four samples of LSG4 (red) compared to the magnetic remanence curves obtained from *vaigre 11* (grey), (b) ESEM micrograph (chemical contrast), (c) Raman microspectroscopy spectrum, (d) diffraction pattern obtained from a LSG4 sample. P = pyrite.

Figure 5: (a) ESEM micrographs (chemical contrast) of a marcasite crystal (*vaigre 11*, wreck of Mandirac), (b), (c), (d), (e), (f) and (g) Framboidal and euhedral pyrite crystals observed by ESEM (chemical contrast) in *vaigre 11* and LSG4 samples.

Figure 6: ESEM micrographs (chemical contrast) of gypsum crystals observed in the wood samples of (a) *vaigre 11*, wreck of Mandirac (b) LSG4. (c) Diffraction pattern of a wood fragment of LSG4. P = pyrite and Gy = gypsum.

Figure 7: ESEM micrographs (chemical contrast) of greigite crystals (a) LSG4 (b) *vaigre 11*, wreck of Mandirac. (c) Typical EDS spectrum obtained from crystals shown on (a).

Table 1: Naturally occurring iron(II) sulfides with oxidation states, magnetic properties (Mrs = Saturation remanence, Hcr = Remanence coercivity, Hsat. = Saturation field, N/A = not applicable) and position of Raman bands (st = strong, m = medium, w = weak, br = broad).

Mineral	**Oxidation state**	**Magnetic properties (single domaine)**			**Raman bands (cm^{-1})**
		Mrs $kA\ m^{-1}$	**Hcr mT**	**Hsat. mT**	
Mackinawite FeS	Fe(+II), S(-II)	N/A	N/A	N/A	nanocrystalline mackinawite [14] : $208_{(m)}$, $282_{(st)}$ well crystallized mackinawite [14] : $208_{(m)}$, $260_{(m)}$, $298_{(st)}$ Fe(III)-containing mackinawite [14] : $125_{(w)}$, $175_{(w)}$, $256_{(m)}$, $312_{(st)}$, $322_{(st)}$, $355_{(m, br)}$
Troilite FeS	Fe(+II), S(-II)	N/A	N/A	N/A	160, 310, 360 [40]
Pyrrhotite $Fe_{1-x}S$ 4C(Fe_7S_8) 5C(Fe_8S_9) 11C($Fe_{10}S_{11}$)	Fe(+II), S(-II)	10-30 [41]	40-100 [41]	500-1000 [41]	Raman inactive, no spectrum [42]

6C($Fe_{11}S_{12}$)					
Greigite Fe_3S_4	Fe(+II,+III), S(-II)	28 [43,44]	50-75 [43,44]	300-500 [43,44]	$138_{(w)}$, $188_{(w)}$, $250_{(w)}$, $350_{(st)}$, $365_{(st)}$ [15]
Smythite Fe_9S_{11}	Fe(+II,+III), S(-II) (?)	23 [45]	40 [45]	300 [45]	No data
Pyrite FeS_2	Fe(+II), S_2(-II)	N/A	N/A	N/A	$342_{(m)}$, $349_{(w)}$, $377_{(m)}$, $428_{(w)}$ [46]
Marcasite FeS_2	Fe(+II), S_2(-II)	N/A	N/A	N/A	$323_{(m)}$, $386_{(m)}$ [47]
Magnetite Fe_3O_4	Fe(+II,+III), 0(-II)	29-65 [48]	18-30 [48]	300 [48]	310, 540, 670 [49]
Maghemite Fe_2O_3	Fe(+III), O(-II)	36-50 [48]	17-23 [48]	300 [48]	350, 512, 665, 730, 1330 [49]

Highlights

- Waterlogged wood-iron assemblies are affected by iron fasteners corrosion influenced by sulfides probably supplied by sulfides producing bacteria
- Greigite an pyrite were detected in the wood of two ancient archaeological shipwrecks through a methodological approach suitable for an exhaustive detection of iron sulfides in an organic matrix
- Greigite was characterized by magnetic measurements methods
- The nature of iron sulfides present in archaeological shipwrecks is related to the duration of the burial in anoxic conditions and of the exposure to sulfides
- Waterlogged archaeological wood-iron assemblies testify of the evolution of iron sulfides in sulfides containing media, starting from the precursor corrosion product mackinawite.

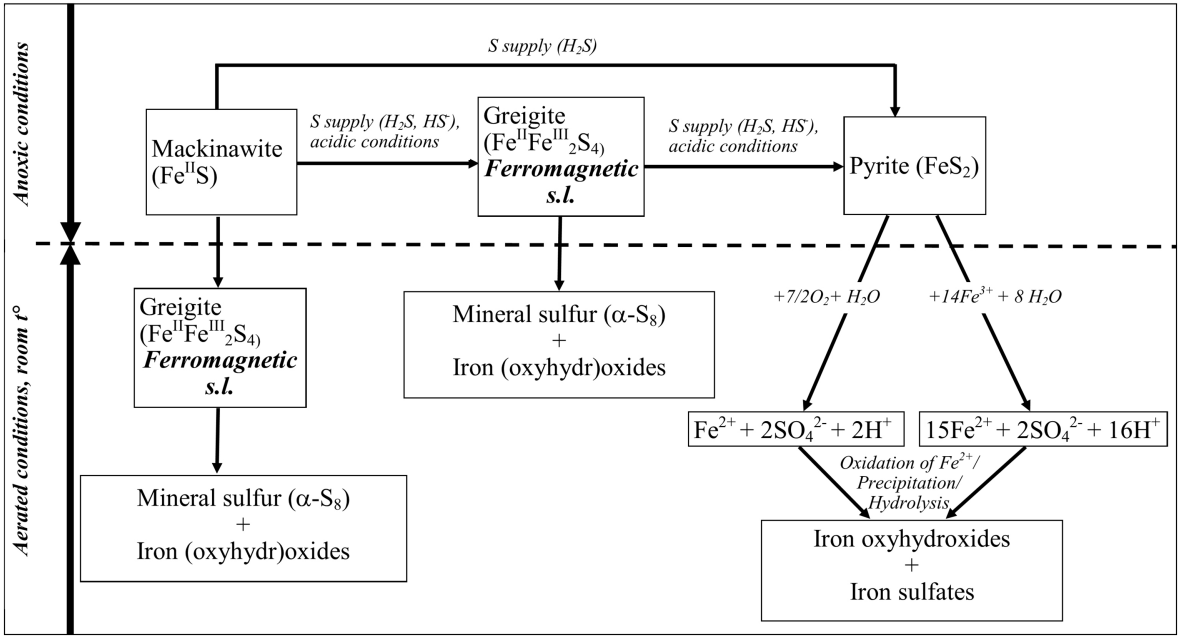
Anoxic conditions
Aerated conditions, room t°
S supply (H_2S)
Mackinawite ($Fe^{II}S$)
S supply (H_2S, HS^-), acidic conditions
Greigite ($Fe^{II}Fe^{III}{}_2S_4$) Ferromagnetic s.l.
S supply (H_2S, HS^-), acidic conditions
Pyrite (FeS_2)
Greigite ($Fe^{II}Fe^{III}{}_2S_4$) Ferromagnetic s.l.
Mineral sulfur (α-S_8) + Iron (oxyhydr)oxides
$+7/2O_2 + H_2O$
$+14Fe^{3+} + 8\,H_2O$
$Fe^{2+} + 2SO_4^{2-} + 2H^+$
$15Fe^{2+} + 2SO_4^{2-} + 16H^+$
Oxidation of Fe^{2+}/ Precipitation/ Hydrolysis
Mineral sulfur (α-S_8) + Iron (oxyhydr)oxides
Iron oxyhydroxides + Iron sulfates

Figure 1

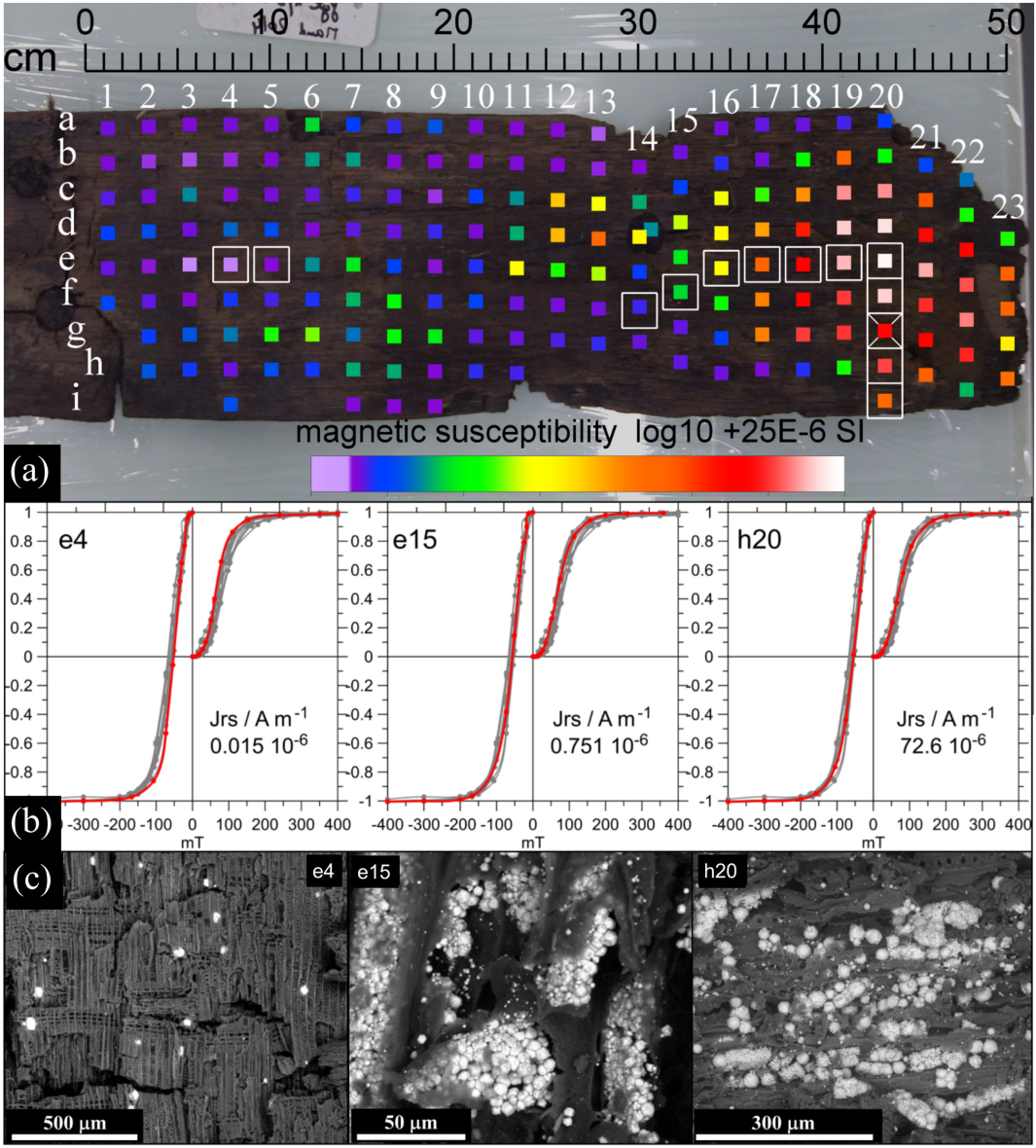
0
10
20
30
40
50
cm
1 2 3 4 5 6 7 8 9 10 11 12 13 14 15 16 17 18 19 20 21 22 23
a
b
c
d
e
f
g
h
i
magnetic susceptibility log10 +25E-6 SI
(a)
e4
Jrs / A m-1
0.015 10-6
e15
Jrs / A m-1
0.751 10-6
h20
Jrs / A m-1
72.6 10-6
mT
(b)
(c)
e4
e15
h20
500 µm
50 µm
300 µm

Figure 2

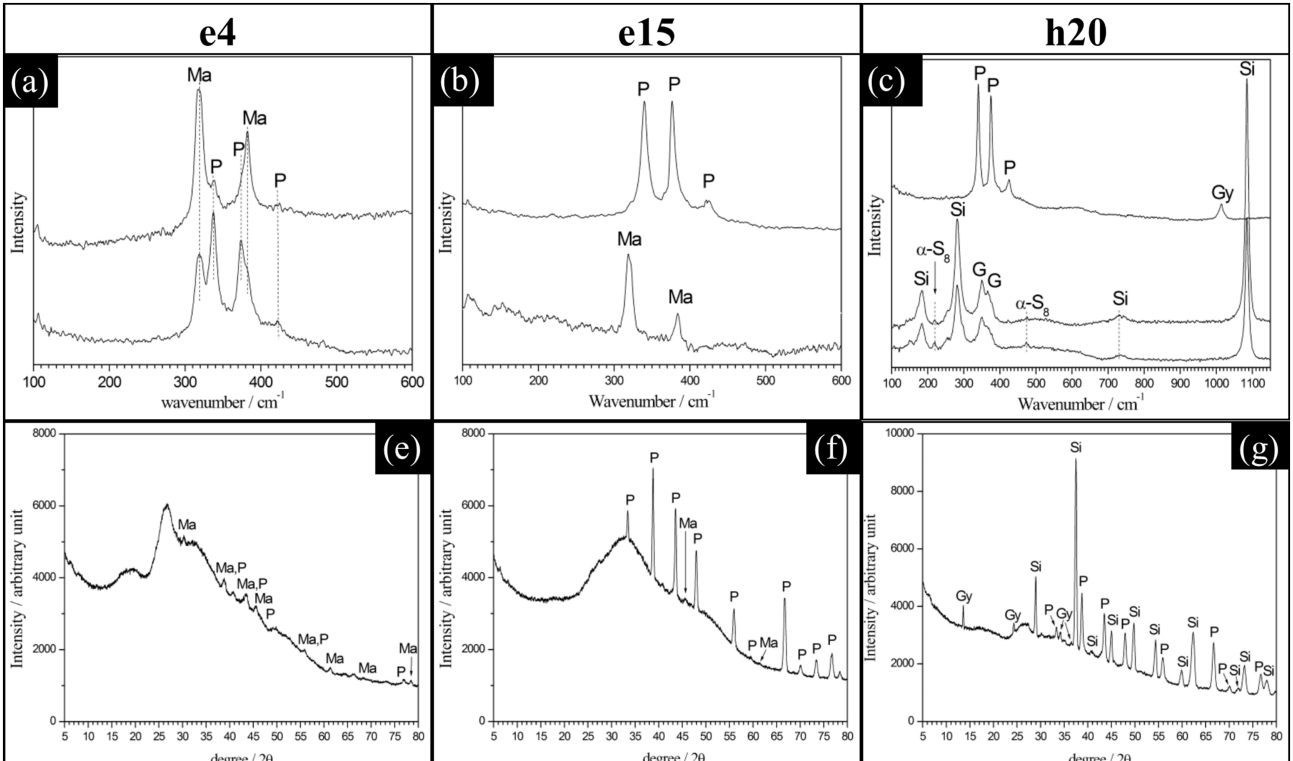
e4
e15
h20
(a)
(b)
(c)
(e)
(f)
(g)
Intensity
wavenumber / cm-1
Wavenumber / cm-1
Intensity / arbitrary unit
degree / 2θ
Ma
P
Si
Gy
α-S8
G

Figure 3

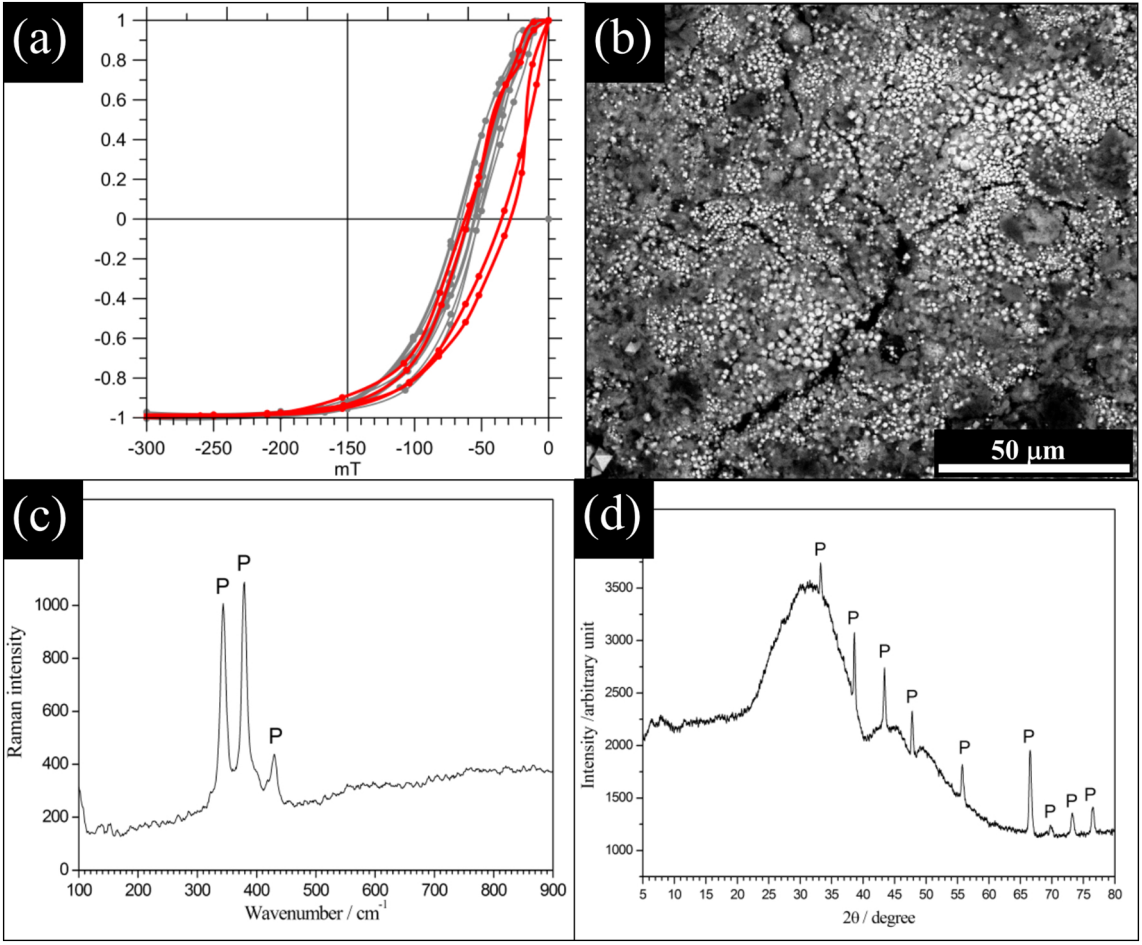
(a)
1
0.8
0.6
0.4
0.2
0
-0.2
-0.4
-0.6
-0.8
-1
-300
-250
-200
-150
-100
-50
0
mT
(b)
50 µm
(c)
P
P
P
Raman intensity
1000
800
600
400
200
0
100
200
300
400
500
600
700
800
900
Wavenumber / cm-1
(d)
P
P
P
P
P
P
P
P
P
Intensity /arbitrary unit
3500
3000
2500
2000
1500
1000
5
10
15
20
25
30
35
40
45
50
55
60
65
70
75
80
2θ / degree

Figure 4

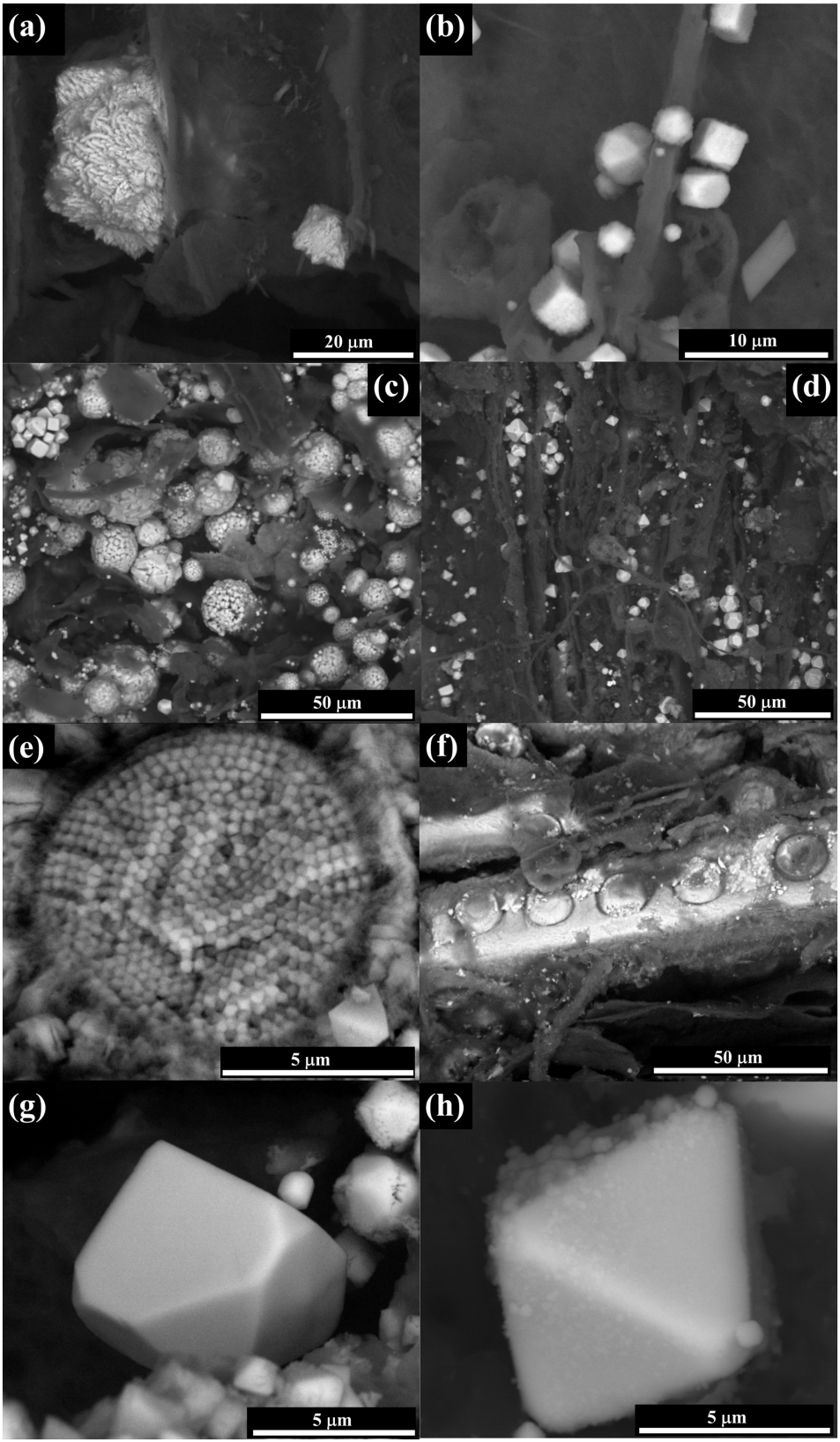

Figure 5

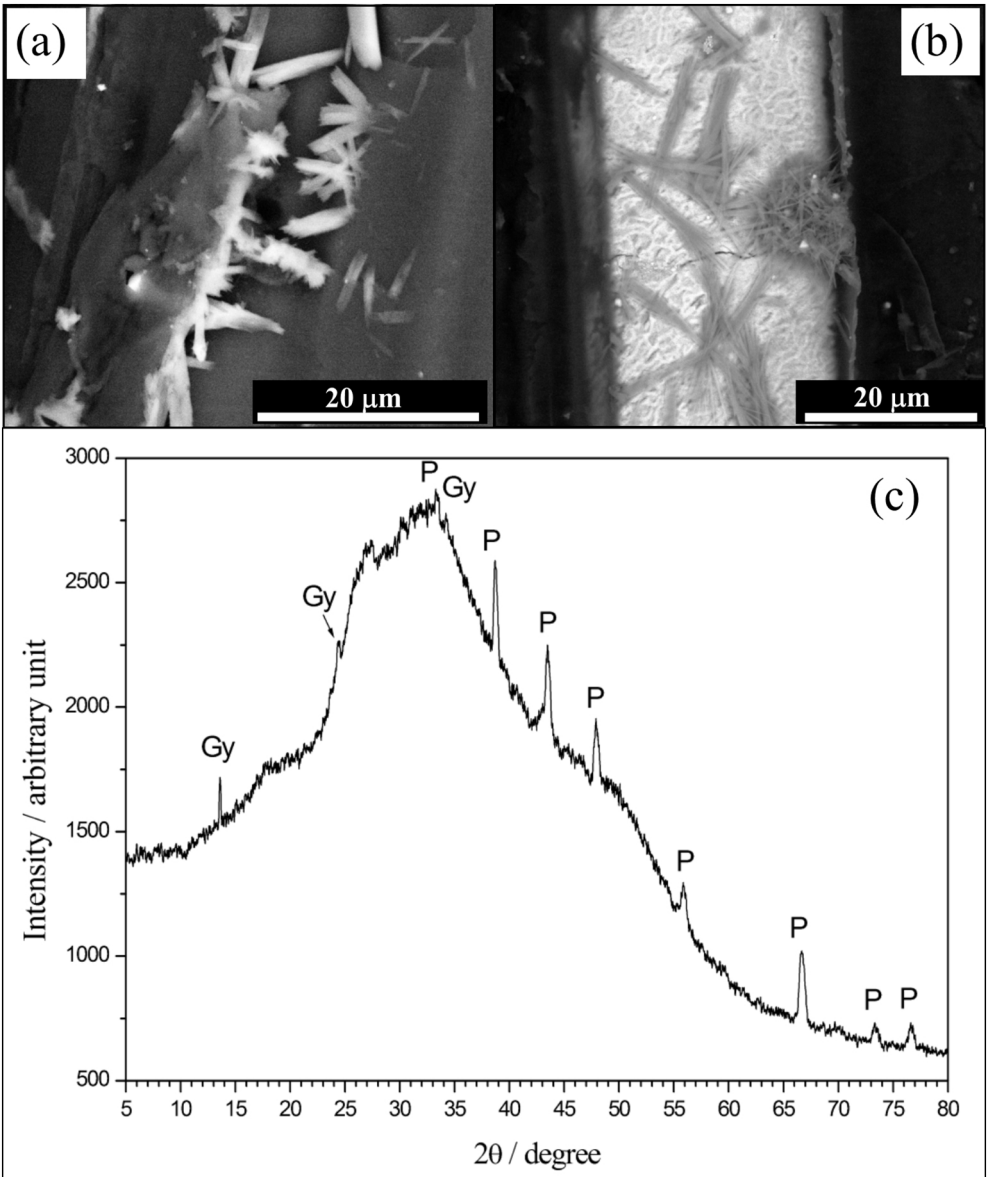
(a)
20 μm
(b)
20 μm
(c)
Intensity / arbitrary unit
2θ / degree
Gy
Gy
P
Gy
P
P
P
P
P
P
P
3000
2500
2000
1500
1000
500
5
10
15
20
25
30
35
40
45
50
55
60
65
70
75
80

Figure 6

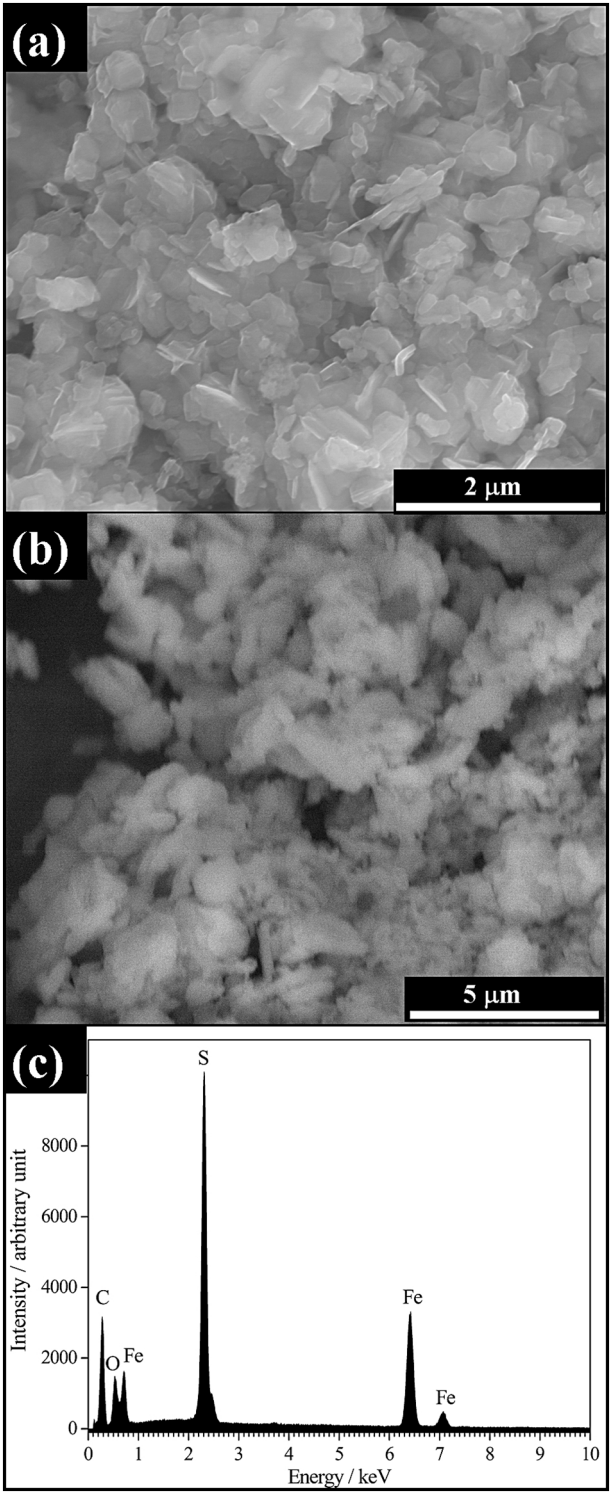
(a)
2 μm
(b)
5 μm
(c)
S
C
O
Fe
Fe
Fe
Intensity / arbitrary unit
8000
6000
4000
2000
0
0
1
2
3
4
5
6
7
8
9
10
Energy / keV

Figure 7